Stability of low-pressure turbine boundary layers under variable Reynolds number and pressure gradient

Alessandro Dotto ✉ 🆔 ; Matteo Luzzi 🆔 ; Jacopo Verdoya 🆔 ; Daniele Simoni 🆔 ; Ardeshir Hanifi 🆔 ;
Jan Oscar Pralits 🆔

Check for updates

CrossMark

View
Online

Export
Citation

Physics of Fluids

Special Topic:
Flow and Civil Structures

Submit Today

AIP Publishing

Stability of low-pressure turbine boundary layers under variable Reynolds number and pressure gradient

Alessandro Dotto,[1,a] (iD) Matteo Luzzi,[1] (iD) Jacopo Verdoya,[1] (iD) Daniele Simoni,[1] (iD) Ardeshir Hanifi,[2] (iD) and Jan Oscar Pralits[3] (iD)

AFFILIATIONS

[1]Department of Mechanical Engineering (DIME), Università degli Studi di Genova, Via Montallegro 1, Genova 16145, Italy

[2]FLOW, Department of Engineering Mechanics, KTH Royal Institute of Technology, 100 44 Stockholm, Sweden

[3]Department of Civil, Chemical and Environmental Engineering (DICCA), Università degli Studi di Genova,
 Via Montallegro 1, Genova 16145, Italy

[a]Author to whom correspondence should be addressed: alessandro.dotto@edu.unige.it

ABSTRACT

The free-stream turbulence induced transition occurring under typical low-pressure turbine flow conditions is investigated by comparing linear stability theory with wind tunnel measurements acquired over a flat plate subjected to high turbulence intensity. The analysis was carried out, accounting for three different Reynolds numbers and four different adverse pressure gradients. First, a non-similarity-based boundary layer (BL) solver was used to compute base flows and validated against pressure taps and particle image velocimetry (PIV) measurements. Successively, the optimal disturbances and their spatial transient growth were calculated by coupling classical linear stability theory and a direct-adjoint optimization procedure on all flow conditions considered. Linear stability results were compared with experimental particle image velocimetry measurements on both wall-normal and wall-parallel planes. Finally, the sensitivity of the disturbance spatial transient growth to the spanwise wavenumber of perturbations, the receptivity position, and the location where disturbance energy is maximized were investigated via the built numerical model. Overall, the optimal perturbations computed by linear stability theory show good agreement with the streaky structures surveyed in experiments. Interestingly, the energy growth of disturbances was found to be maximum for all the flow conditions examined, when perturbations entered the boundary layer close to the position where minimum pressure occurs.

Published under an exclusive license by AIP Publishing. https://doi.org/10.1063/5.0188024

I. INTRODUCTION

Boundary layer (BL) transition always had major attention in aeronautics and turbomachinery research, where lots of efforts are paid by the scientific community to get further insight into the mechanisms governing boundary layer stability and its transition routes. In the case of an attached laminar boundary layer (BL), depending on the free-stream turbulence (FST) intensity, both the ordinary (i.e., *natural transition*) and the *FST induced*—formerly *bypass*—transition mechanisms may occur.[1] Specifically, the natural transition caused by the amplification of Tollmien–Schlichting waves occurs at low free-stream turbulence intensity levels $Tu < 1\%$, whereas the FST induced route dominates flow conditions characterized by larger Tu. Given the quite high turbulence intensity characterizing the flow around turbine and compressor blades, traditionally the focus on transition in the

turbomachinery field is posed mainly on the bypass route. Indeed, fully understanding and foreseeing this transition phenomenon has become a fundamental requirement to manufacture lightweight and aerodynamically efficient low-pressure turbines for modern aircraft engines.[2] In this case, the transition breakdown is triggered by the instability of streamwise oriented, elongated vortical filaments called *streaks*, which were first observed by Klebanoff *et al.*[3] and Klebanoff.[4] *Streaky structures* appear as low-frequency perturbations of the streamwise velocity, whose unstable evolution and consequent breakup prompt/initiate the formation of turbulent spots.[5–7] When the flow is still laminar, low-frequency disturbances embedded within the free stream penetrate into the boundary layer, in a receptivity process termed *shear-sheltering*,[8,9] thus generating streaks. As streaks evolve along the streamwise direction, their amplitude grows and their spanwise size

approximately matches the boundary layer thickness. When streaky disturbances are sufficiently strong, they become unstable and breakup via secondary instability mechanisms.[10,11]

Differently from the natural transition, the bypass route relies on the non-modal transient growth of disturbance energy, up to trigger secondary instabilities and turbulence breakdown (see, e.g., Hoepffner et al.[5] Schlatter et al.[12]). For this reason, asymptotic analyses are incapable of capturing the FST induced boundary layer transition, whereas linear stability theory coupled with a direct-adjoint optimization procedure is typically adopted to evaluate the shape and transient growth of optimal disturbances.[13] Previous studies explored the potential of this technique for relatively simple flows, such as Blasius's[13–16] or Falkner–Skan–Cooke's (FSC)[17,18] boundary layer similarity solutions. Despite considering relatively simple flow conditions, most of the current literature successfully analyzed the impact of crucial parameters on the FST-induced transition. In particular, Andersson et al.[13] showed that increasing the Reynolds number Re causes higher energy amplification for the streaky disturbances, with perturbation growth G scaling linearly with Re for $Re > 10^5$. Additionally, for a Zero Pressure Gradient (ZPG) boundary layer, Andersson et al.[13] found that, when G is maximized with respect to the initial (x_i) and final (x_f) positions of the disturbance evolution along the flow path, the energy gain shows a maximum against x_f itself, where turbulent breakdown is expected to occur. Successively, Levin and Henningson[16] observed a maximum trend of G with respect to the receptivity location x_i, i.e., the position at which the disturbance enters the boundary layer, with higher amplification of disturbances achieved introducing perturbations downstream of the flt plate leading edge. Finally, by investigating the influence of pressure gradients on perturbation growth in FSC boundary layers, Andersson et al.[7] showed that increasing adverse pressure gradients (APGs) determines higher values for G. Nevertheless, the well-known numerical instability of the FSC similarity solutions for specific values of the Hartree's parameter constrained the analysis on weak APGs.

However, few attempts have been made in the literature toward the application of linear stability theory and direct-adjoint optimization to complex, non-similarity-based boundary layer flows, such as those occurring over wing airfoils or turbomachinery blades.[19–21] Most noticeably, Mao et al.[22] applied linear stability theory to find out optimal perturbations for boundary layer developing over a NACA 65 airfoil, typically used for compressor blades. The present work aims to add knowledge to the current scenario and investigate the free-stream turbulence induced transition in boundary layer flows typically occurring over highly-loaded low-pressure turbine (LPT) blades of modern aeroengines.[23–25] The analysis is carried out by means of a numerical model employing linear stability theory and wind tunnel experimental data. More specifically, a completely general (i.e., non-similarity-based) boundary layer solver has been used to solve for base flows, which are characterized by strong APGs following the channel throat. Different Reynolds number and APG flow conditions were reproduced by the boundary layer solver and validated against wall-normal particle image velocimetry (PIV) measurements, thus demonstrating the accuracy of the numerical procedure. Successively, linear stability theory was applied to calculate optimal disturbances through direct-adjoint optimization approach. The method employed was proven in the literature[13,16] as a capable mean of simulation, despite its simplicity. While a direct numerical simulation (DNS) would have provided a full description of the flow field, the employed method can achieve meaningful

results in significantly less time and effort, making it still affordable for the scientific community at all levels. Results were again compared with experimental data, this time against wall-parallel PIV measurements. Overall, the analysis provides useful insight into the transition mechanisms occurring in complex, turbomachinery boundary layer flows. The next Sec. II introduces the experimental setup and measurement techniques adopted in this work, whereas insights into the numerical procedure used are reported in Sec. III. In Sec. IV A, the numerical base flows are validated against PIV experimental data for a wide number of APG conditions and streamwise positions. Finally, in Secs. IV B and IV C, results regarding the optimal disturbances provided by linear stability theory are compared with experimental evidence by numerically varying critical parameters (x_i, x_f, Re, APG,...), which influence the spatial transient growth of a streaky structure. Overall, the results of the present manuscript can significantly contribute to the understanding of the physical mechanisms underlying the bypass transition and to the formulation of simple but accurate approaches for its investigation, which should provide significant benefits for the aerodynamic sector, especially for aeroengine technology.

II. EXPERIMENTAL SETUP AND MEASUREMENTS
A. Test section and examined flow conditions

The experimental campaign was carried out in the low-speed open-loop wind tunnel of the Aerodynamics and Turbomachinery Laboratory at the University of Genoa. The test section comprises a 20 mm thick, 300 mm long, and 300 mm wide flat plate, ensuring 2D time-mean flow at mid-span with negligible end effects.[23] The flat plate has a 4:1 elliptic nose, designed to prevent leading edge separation. The following fore portion of the test section has a fixed converging geometry up to the geometrical throat of the channel (positioned at $x/L = 0.20$, L being the plate length), whereas two adjustable endwalls provide prescribed APGs over the flat plate (see Fig. 1). Three optical accesses to the flat plate are granted through plexiglass panels on the sides and on the top surface of the test section. A tripwire installed on the top and the bottom end-walls at the channel throat is used to prevent uncontrolled boundary layer laminar separation along these surfaces, hence ensuring that the correct Diffusion Rate (DR) is imposed to the flat plate boundary layer.
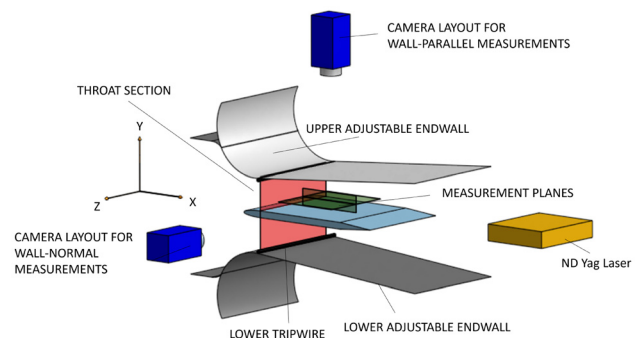
FIG. 1. Depiction of the test section and PIV instrumentation layout. Wall-parallel and wall-normal measuring planes are highlighted in green; the geometric throat in red. The adjustable end-walls above and below the flat plate are shown at a 5° opening angle: here, trip wires are placed near the throat.

The setting and control of the proper angle of attack for the different conditions can be surveyed by 17 pressure taps symmetrically distributed on the top and bottom sides of the leading edge curved surfaces—a first measurement tap is placed on the foremost point of the nose. Additionally, 51 equally spaced pressure taps installed on the horizontal section of the plate were used to characterize the pressure gradient imposed in this region by different end wall settings. The achieved pressure gradient is quantified by the diffusion rate DR defined in Eq. (1), with U_{th} being the peak velocity in the throat, L being the plate length, and $\Delta U/\Delta x$ being evaluated in the diffusing region of the test section—i.e., the part of the test section dealing with adjustable, diverging end-walls,

$$DR = \left| \frac{\Delta U}{\Delta x} \right| \frac{L}{U_{th}}. \tag{1}$$

By employing definition (1) Re_L—based on the flat plate length—and APG can be effectively considered as independent variables in setting up the test matrix of flow conditions analyzed in this work. Top end-wall opening angles of $1°$, $5°$, $9°$, and $12°$ have been adopted in the experimental campaign, corresponding to DR of 0.00, 1.30, 2.10, and 2.30. FST is controlled using a turbulence generator, positioned 500 mm upstream of the flat plate, which ensures a turbulence intensity of 5% at its leading edge. The desired turbulence intensity level is obtained using a grid of squared bars, having a mesh size of 10 mm and a bar width of 10 mm and therefore a porosity parameter $\beta_P = 0$. Further details on the dependence of Tu levels on the geometric features of turbulence generating grids can be found in Verdoya et al.[26] Thanks to the described setup, the free-stream turbulence intensity, the Reynolds number, and the aerodynamic load distribution in the test reproduce those of an LPT blade, as the boundary layer is subjected to pressure gradients and turbulence intensity typically occurring in low-pressure turbine flows. All combinations of three Reynolds numbers—based on the plate length and the free-stream velocity at the plate leading edge, $Re_L = 70$ k, 150 k, 220 k—and the four aforementioned diffusion rates were tested in the present work. Twelve flow conditions were examined in total, at fixed $Tu = 5\%$.

B. Measurement techniques

Experimental data were collected utilizing a Dantec time-resolved PIV system. The instrumentation consists of a dual-cavity Nd:YLF pulsed laser Litron LDY 300 (energy 30 mJ per pulse at 1000 Hz repetition rate, 527 nm wavelength). The optics generate a light sheet of 1 mm thickness. The laser light is scattered by Vaseline oil droplets with a mean diameter of 1.5 μm, and it is captured by a high-sensitive SpeedSense M340 digital camera with a cooled 2560 × 1600 pixels CMOS matrix. This setting results in a particle image diameter of the order of three pixels, with a seeding concentration of around four to five particles for the investigation area. Given the considerably small diameter of the Vaseline droplets, it is safe to assume that the particles remain suspended indefinitely during the experiment. The adaptive cross correlation with a peak validation algorithm was used over an interrogation area of 16 × 16 pixels with a 50% overlap, resulting in a vector spacing of less than 0.5 mm and an estimated error on velocity measurements lower than 3%, as verified in the error estimation for a similar setup by Dellacasagrande et al.[27] A

formal description of the computation of the accuracy of the PIV measurement system can be found in the analyses of Sciacchitano et al.[28] and Wieneke.[29]

PIV measurements were acquired independently on a wall-normal and on a wall-parallel plane, embedded in the boundary layer at around $y/\delta_{99} \approx 0.5$, at $x/L = x_0^*$. The location and the magnification factor of both PIV measurement planes were determined by acquiring the images of a calibrated target before each acquisition. At this stage, minor uncertainty sources such as plexiglass refraction of light and relative placement of cameras and test section were addressed and showed to have negligible impact on results. The PIV frame in the wall-normal plane extends from $x/L = 0.27$ to $x/L = 0.81$ in the streamwise direction, focusing from the plate surface up to $y/L = 0.04$ in the free-stream region—L being the flat plate length. The field of view allows us to capture the boundary layer evolution in the streamwise direction, and thus, the overall characterization of the transition process depending on the flow conditions. Eight independent data sets of 2000 PIV snapshots were acquired at a sampling rate of 2 kHz in this plane, providing a good convergence of the boundary layer statistical quantities for each of the flow conditions tested. The PIV field of view of the wall-parallel plane covers the region from $x/L = 0.33$ to $x/L = 0.83$, spanning 1/3 of the flat plate width and centered at the mid-section. This allows the visualization of the population of alternating high- and low-speed streaks developing in the transitional boundary layer and the characterization of their spanwise wavelength, ultimately providing an evaluation of the experimental disturbance, as demonstrated in Verdoya et al.[30]

III. MATHEMATICAL PROCEDURE

Free-stream turbulence induced transition is investigated by applying linear stability theory to a boundary layer numerical solution. To this end, the incompressible, steady-state Navier–Stokes equations are decomposed by a superposition of a 2D boundary layer mean flow $(U, V, 0) = (U(x,y), V(x,y), 0)$ and 3D disturbances (u, v, w, p) $= (u(x,y,z), v(x,y,z), w(x,y,z), p(x,y,z))$. According to Levin and Henningson,[16] perturbations have been assumed of the form $(u, v, w, p) = (\hat{u}(x,y), \hat{v}(x,y), \hat{w}(x,y), \hat{p}(x,y))e^{i\beta z}$, i.e., with zero time frequency, periodic in the spanwise direction z and amplifying along the streamwise and wall-normal directions x and y. Following the formulation of Andersson et al.,[13] an appropriate scaling for algebraically growing disturbances and base flows is adopted, as summarized in Table I. In detail, L_{ref} measures the distance ranging from the leading edge of the flat plate to the throat position; hence, the Reynolds number is consequently defined as $Re = U_{ref} \cdot L_{ref}/\nu$; δ represents the boundary layer thickness and β is the spanwise wavenumber of perturbations. Provided the scalings reported in Table I, the non-dimensional linearized Navier–Stokes equations for the disturbances can be expressed as

TABLE I. Base flow and disturbance scalings. The subscript *ref* refers to the minimum cross-flow area of the test section (i.e., the geometrical throat).

x	y,z	t	$U, \hat{u}$	$V, W, \hat{v}, \hat{w}$	$P, \hat{p}$	β
L_{ref}	δ	L_{ref}/U_{ref}	U_{ref}	$U_{ref} \cdot \delta/L_{ref}$	$\rho \cdot (U_{ref} \cdot \delta/L_{ref})^2$	δ^{-1}

$$\hat{u}_x + \hat{v}_y + i\beta\hat{w} = 0,$$

$$U_x\hat{u} + U\hat{u}_x + V\hat{u}_y + U_y\hat{v} + \frac{\hat{p}_x}{Re_\delta^2} = \hat{u}_{yy} - \beta^2\hat{u},$$

$$V_y\hat{v} + U\hat{v}_x + V_x\hat{u} + V\hat{v}_y + \hat{p}_y = \hat{v}_{yy} - \beta^2\hat{v}, \qquad (2)$$

$$U\hat{w}_x + V\hat{w}_y + i\beta\hat{p} = \hat{w}_{yy} - \beta^2\hat{w},$$

where $Re_\delta = U_{ref}\delta/\nu$ and higher order terms (i.e., $O(1/Re_\delta^2)$) have been neglected. The boundary conditions for this problem are no-slip and vanishing disturbances in the wall-normal direction at $y = 0$ and $y = y_{max}$, respectively,

$$y = 0 : (\hat{u}, \hat{v}, \hat{w}, \hat{p}) = (0,0,0,0),$$
$$y = y_{max} : (\hat{u}, \hat{v}, \hat{w}, \hat{p}) \to (0,0,0,0). \qquad (3)$$

Furthermore, since the complex geometry of the test section does not allow for similarity flow conditions, the 2D mean flow $(U, V, 0)$ in Eq. (2) has been obtained numerically by solving boundary layer equations for generic flows, without introducing similarity hypotheses.[31] The main purpose of the boundary layer solver is to provide high-fidelity numerical results next to the leading edge of the flat plate, i.e., outside the PIV measurement domain, and to accurately match the experimental data where directly available. It must be remarked here that the boundary layer solver neglects the turbulent momentum transfer from the free-stream and only relies on laminar flow equations; thus, incipient flow separation may be detected by it in the case of adverse pressure gradient, even though the actual non-zero turbulence level present in experiments keeps the flow attached. By adopting a second order finite difference and Chebyshev discretization schemes along x and y, respectively, the matrix form of the parabolized stability equations (PSEs) (2) has been derived:[31]

$$q_f = \mathcal{L}q_i, \qquad (4)$$

where $\mathcal{L}$ is the non-dimensional linearized Navier–Stokes operator providing the disturbance evolution along x, whereas $q_i = (\hat{u}, \hat{v}, \hat{w}, \hat{p})|_{x_i}$ and $q_f = (\hat{u}, \hat{v}, \hat{w}, \hat{p})|_{x_f}$ are the disturbance amplitudes at x_i and x_f for the perturbation evolution, respectively. In Eq. (4), no-slip condition at $y = 0$ and vanishing disturbance at $y = y_{max}$ have been implemented in the matrix form. Therefore, once a general disturbance shape is provided at x_i, Eq. (4) computes its evolution step-by-step along the streamwise direction from x_i to x_f. Hence, to identify the optimal disturbance, i.e., the disturbance introduced at x_i whose energy is maximized at a certain x_f, the following optimization problem needs to be solved:[31]

$$G_{max} = \max_{q_i}\frac{\|q_f\|^2}{\|q_i\|^2} = \max_{q_i}\frac{\|\hat{u}_f\|^2}{\|q_i\|^2}, \qquad (5)$$

where $G = \|q_f\|^2/\|q_i\|^2$ represents the spatial transient growth of the perturbation evolving from x_i to x_f. In Eq. (5), the wall-normal and spanwise components of q_f are neglected and the squared norm is defined as $\|q\|^2 = \int_0^{y_{max}}(\mathrm{Re}|u|^2 + |v|^2 + |w|^2)dy$. To solve the optimization problem (5), an iterative adjoint optimization procedure has been set up, according to previous works in the literature.[16,32] By definition, the adjoint $\mathcal{L}^*$ of an operator $\mathcal{L}$ satisfies

$$\langle a, \mathcal{L}d \rangle = \langle \mathcal{L}^*a, d \rangle, \qquad (6)$$

where $d = d(x, y)$ and $a = a(x, y)$ are the direct and adjoint variables, respectively, whereas $\langle \cdot, \cdot \rangle$ denotes an inner product. In the present

work, this is defined as $\langle d, a \rangle = \int_x\int_y d^T a\,dy\,dx$, where the apex T denotes the conjugate transpose. Based on the definition of the adjoint operator, the following system for the adjoint perturbation $q^* = (p^*, u^*, v^*, w^*)$ is derived:

$$-v_y^* + i\beta w^* = 0,$$

$$-Uu_x^* - V_y u^* - Vu_y^* + V_x v^* - p_x^* = u_y y^* - \beta^2 u^*,$$

$$-Uv_x^* - U_x v^* - Vv_y^* + U_y u^* - p_y^* = v_y y^* - \beta^2 v^*, \qquad (7)$$

$$-Uw_x^* - Vw_y^* + i\beta p^* = w_y y^* - \beta^2 w^*,$$

or, in the matrix form,

$$q_i^* = \mathcal{L}^* q_f^*. \qquad (8)$$

Equation (8) is obtained by adopting the same discretization schemes along x and y used for Eq. (4). Due to the negative sign of the x derivative, the adjoint problem (7) is to be solved marching from x_f to x_i and adopting $q_f^* = (\hat{u}_f, 0, 0, 0)$ as the initial condition at x_f.[16,31] Overall, by introducing the definition of the adjoint operator, the optimization problem (5) becomes

$$\max_{q_i}\frac{\langle\mathcal{L}^*\mathcal{L}q_i, q_i\rangle}{\langle q_i, q_i\rangle}, \qquad (9)$$

whose solution has been obtained by means of power iterations,

$$q^{j+1} = \mathcal{L}^*\mathcal{L}q^j. \qquad (10)$$

Here, q^j and q^{j+1} represent the optimal disturbances at the j-th and $j + 1$-th iteration steps, respectively, which are updated by sequentially solving the direct and adjoint systems. Iterations continue until $\frac{G^{j+1}-G^j}{G^j} < \varepsilon$, where ε is an arbitrary infinitesimal threshold. More details on the numerical procedures used in this work can be found in the Appendix, whereas a complete treatment is available in Hanifi *et al.*[31]

IV. RESULTS

In this section, numerical results are presented against experimental data, employing a different non-dimensional scaling to the boundary layer solver one reported in Table I. In the following, the flat plate extent L and the free-stream velocity U_{th}, measured at the geometric throat (i.e., $x/L = 0.20$), will be used as the length and velocity scales, aiming to a more compliant comparison between numerical and experimental works. The updated scaling is summarized in Table II, where δ^* and θ indicate the boundary layer displacement and momentum thickness, respectively. All the quantities shown in the diagrams included in the following sections are made non-dimensional through the scaling reported in Table II.

A. Base flow comparison

A comparison of the boundary layer solver results against measurements is performed first to validate its accuracy in reproducing

TABLE II. Scalings used for reporting results in non-dimensional form.

x, y, z	t	$U_e, U, \hat{u}, u'$	δ^*, θ	β
L	L/U_{th}	U_{th}	L	$1/L$
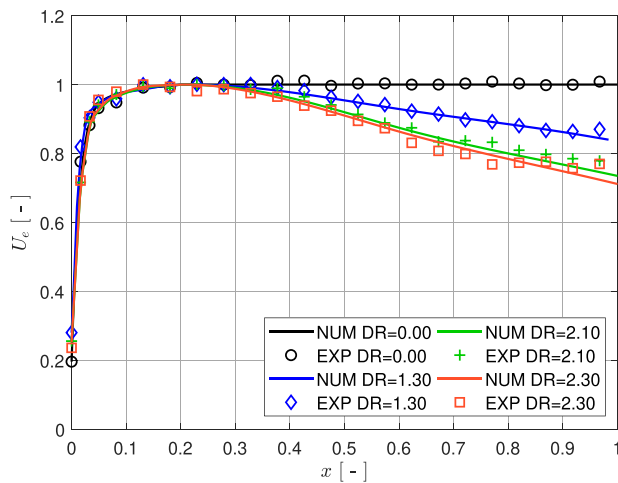
FIG. 2. Dimensionless free-stream velocity distributions obtained by means of pressure taps (markers)—using a 1:3 skip for graphical readability—and fitted distribution (solid lines) for varying DR at fixed $Re_L = 70$ k. The reported non-dimensional plots follow the scaling indicated in Table II.

experimental data. Free-stream velocity, boundary layer profiles, and integral parameters are presented for each DR at the lowest Reynolds number in the analysis—i.e., 70 k. For each combination of DR and Re_L, the distribution of the pressure coefficient $C_p = 2(p - p_\infty)/(\rho U_\infty^2)$—with U_∞ being the free-stream velocity measured far upstream the leading edge—was surveyed via pressure taps. The resulting free-stream velocity distributions $U_e(x)/U_{th}$ are summarized in Fig. 2 for each DR. Experimental data are shown only for the case $Re_L = 70$ k for the sake of conciseness. Markers show the reference free-stream velocity evolution gathered from C_p measurements, while continuous curves denote the numerical fitting of experimental data, which has been set as a free-stream boundary condition in the BL solver (see Sec. III). Using interpolated data instead of the experimental ones allows the numerical solver to accurately determine boundary layer profiles and ultimately provide a second-order-differentiable pressure distribution along the streamwise direction. Figure 2 highlights how variable DR does not affect the forepart of the free-stream flow since the geometry is fixed up to the geometrical throat—outlined in Sec. II. On the other hand, the adverse pressure gradient effect substantially reduces the free-stream velocity downstream of $x/L = 0.20$. Imposing a 1° end-wall opening angle determines a nearly constant $U_e(x)$ downstream of the throat, compensating for the weak flow acceleration in the free stream caused by the boundary layer growth along the flat plate. All the curves show the attached flow, even at the strongest DR, thanks to the high inlet FST intensity level ($Tu = 5\%$) imposed in the experiments, which helps in preventing separation in all the surveyed configurations.

Figure 3 shows the experimental measurement and numerical boundary layer profiles from the BL solver. The comparison is carried out at three different streamwise locations for variable DR, $Re_L = 70$ k. Higher Reynolds numbers—$Re_L = 150$ k and $Re_L = 220$ k—provided essentially the same level of agreement and are not reported here for brevity—please refer to Kubacki et al.[33] and Dellacasagrande et al.[27] for details over the Reynolds range on the flow field employed also in this study. Experimental and numerical BL profiles for the ZPG flow

nearly coincide up to $x/L = 0.45$. Downstream of this position, the experimental boundary layers become transitional, especially over $x/L = 0.55$. Progressively higher $DR = 1.30$, 2.10, and 2.30 show that the numerical boundary layers start differing from the experimental ones earlier—downstream of $x/L = 0.45$, 0.40, and 0.35, respectively. This discrepancy at high streamwise coordinates is due to the boundary layer solver, neglecting the turbulent momentum transfer from the free-stream (see Sec. III). Hence, it detects incipient flow separation if significant APGs are imposed. Interestingly, the predicted separation location moves upstream as DR increases, coherently with the expected flow physics and further proving the reliability of the solver. Instead, the experimental profiles remain attached and show transitional features at the same streamwise position x. However, it is well known from the literature that the receptivity for algebraically growing disturbances occurs at earlier streamwise locations in the BL (see, e.g., Hammerton and Kerschen[34] and Lin et al.[35]); thus, the boundary layer comparison holds with good agreement in the flow regions where streak formation and amplification occur. As such, in Sec. IV C, stability analysis for the spatial transient growth of perturbations will focus on $x/L \leq 0.40$, i.e., where good agreement is achieved for base flows. Numerical profiles in this region were used to calculate optimal disturbances to benefit from better resolution compared to experimental results.

Figure 4 reports the perturbation profiles computed by the adjoint optimization and the experimental *rms* of streamwise velocity fluctuations from PIV measurements on the wall-normal plane. The comparison is performed on the same flow conditions and streamwise locations reported in Fig. 3. Both numerical and experimental profiles are normalized by their respective maximum in the wall-normal direction. Indeed, it has been shown via different independent experimental studies in the literature over time[36–39] that the rms fluctuations of velocity tend to similar profile shapes almost independently of the free-stream turbulence intensity applied. Overall, a remarkable correspondence between the shape of numerical and experimental profiles is observed, especially concerning the cases at low DR and near the throat. However, it should be noted that beyond the BL edge (i.e., within the free-stream flow), the numerical profiles significantly differ (20–50% gap) from the experimental ones. This is a direct consequence of the vanishing disturbance boundary conditions implemented at $y \to \infty$ in the linear stability model, according to Dotto et al.[40] Instead, vortices in the actual free-stream result in non-null perturbation amplitudes outside of the boundary layer, as captured by the experimental measurements. Finally, a few discrepancies in the rms profile shape arise at higher streamwise coordinates (blue lines) in the case of nonzero APG. Specifically, experimental results show that increasing DR pushes the maximum of rms closer to the wall, compared to the numerical prediction.

However, the observed discrepancies are in line with other works from the literature.[7,38,41] Thus, the few differences in Fig. 4 for the nonzero DR conditions were deemed reasonable. The momentum (θ) and displacement (δ^*) thicknesses calculated from the BL solver are shown in Fig. 5 together with experimental measurements under the same DR and Re_L of Fig. 3. Experimental integral parameters are provided with error bars representing the PIV measurement uncertainty, as reported in detail in Dellacasagrande et al.[27] The numerical solver integral parameters fall within the experimental accuracy for $DR = 0.00$ and x/L up to 0.60. Interestingly, the numerical δ^* and θ at $DR \geq 1.30$
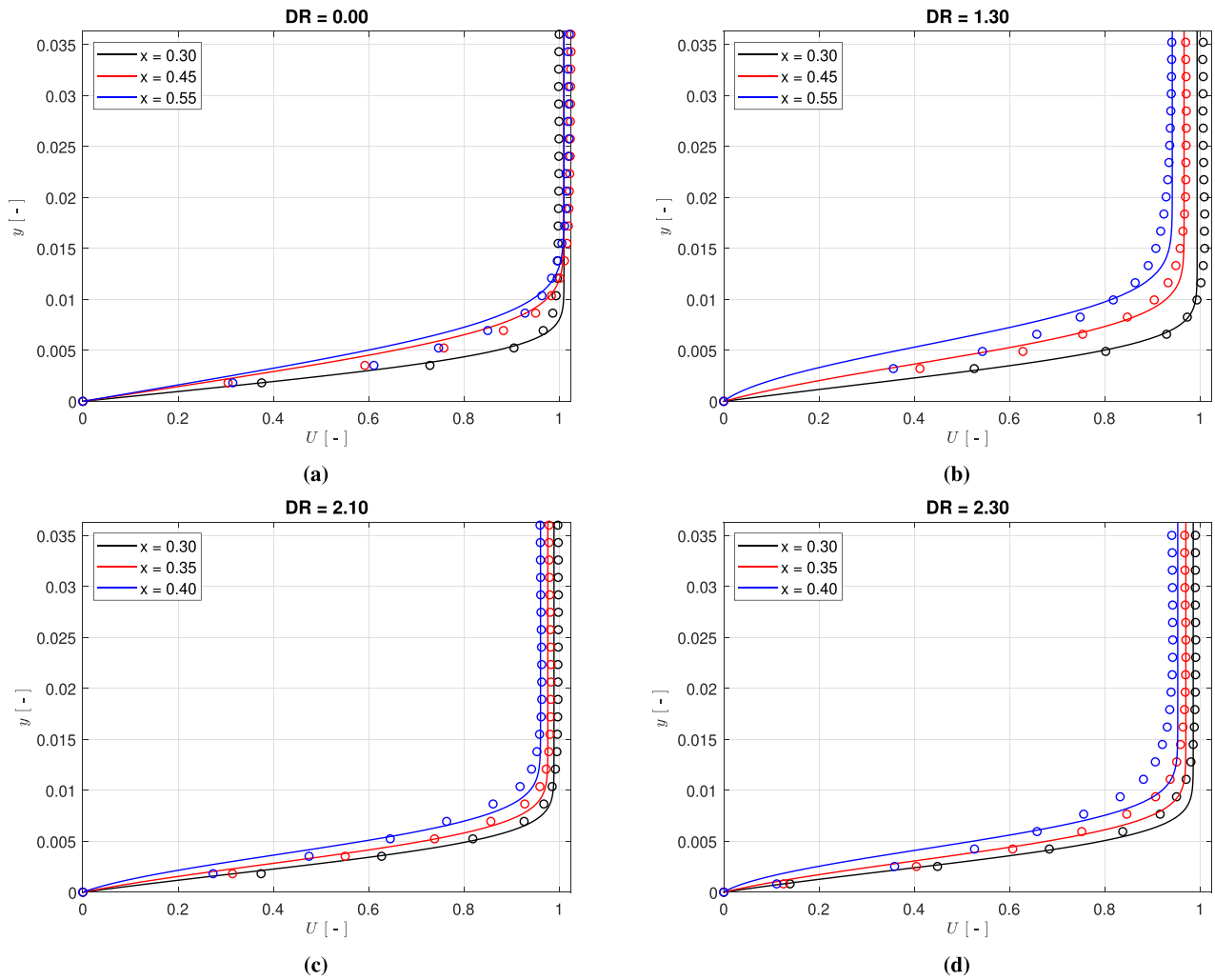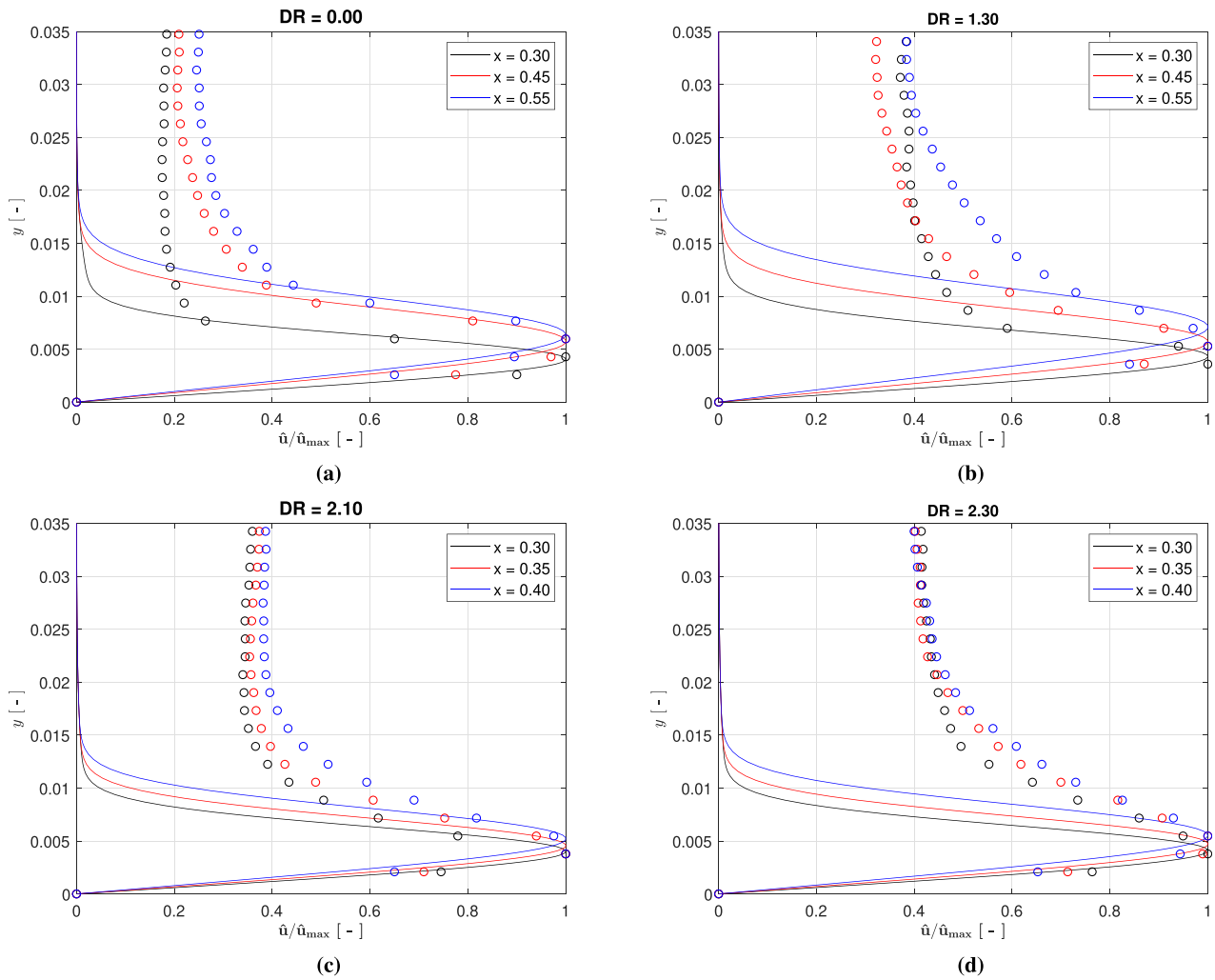
FIG. 3. Boundary layer streamwise velocity profiles obtained by means of time-average PIV measurements (markers) and by the boundary layer solver (solid lines). Curves for $Re_L = 70$ k, (a) $DR = 0.00$, (b) 1.30, (c) 2.10, and (d) 2.30. The reported non-dimensional plots follow the scaling indicated in Table II.

cope well with experimental data in the forepart of the PIV domain (i.e., $x/L \leq 0.38$), despite the high Tu level characterizing the measurements. However, in all cases, the displacement thickness grows faster for the velocity profiles established from the BL solver against the experimental testing toward the end of the computational domain (i.e., $x/L \geq 0.38$) and even more pronounced downstream to where the numerical boundary layers become inflectional. As expected, numerical results for all the investigated DRs start detaching from experimental data in a location close to where the boundary layer profiles begin to differ (see Fig. 3). Nevertheless, this further stresses the reliability of the solver in the former part of the domain, where streaky structures are expected to be generated and amplified. The present comparison of the base flow properties shows that the boundary layer solver reproduces low-pressure turbine boundary layers accurately for variable DRs and Re_L, especially upstream of the position where the non-linearities related to transitional flow take place.

B. Spanwise wavelength and energy growth of the experimentally surveyed perturbations

A qualitative view of the experimentally surveyed disturbances is given in Fig. 6, which depicts PIV snapshots sampled on a wall parallel plane embedded within the boundary layer. Snapshots are reported for three successive time instants: t_0, $t_1 = t_0 + \Delta t$ and $t_2 = t_0 + 2\Delta t$. The time interval Δt differs among all the three rows according to the physical timescale of streak evolution, which is influenced by both Re_L and DR. The contour plot of streamwise velocity fluctuations is superimposed on the perturbation velocity vectors to highlight the occurrence of streaky structures and vorticity nuclei in the reported snapshots. Depending on inflow conditions, the field of view is centered at different streamwise coordinates to better appreciate the wavelength characterizing the structures captured by each acquisition. Focusing on the snapshots concerning $DR = 0.00$ and $Re_L = 70k$, Fig. 6 (top row) shows a population of streamwise elongated structures, consisting of

15 March 2024 08:41:24

FIG. 4. Non-dimensional boundary layer streamwise perturbations profiles obtained by means of rms of the streamwise velocity fluctuation from PIV measurements (markers) and by the boundary layer solver disturbance energy (solid lines). Curves for $Re_L = 70$ k, (a) $DR = 0.00$, (b) 1.30, (c) 2.10, and (d) 2.30. The reported plots follow the scaling indicated in Table II.

positive (red) and negative (blue) velocity fluctuations alternating in the spanwise direction z. A low-speed streak undergoing a regular oscillation during its downstream evolution is detected around $z/L = 0.02$ over all the three successive time instants t_0, t_1, and t_2 sampled for the $DR = 0.00$ and $Re_L = 70k$ flow condition. The third frame also shows two high-speed streaks (red), which start to interact and form a localized turbulent region around $x/L = 0.60$. Increasing the flow Reynolds number under fixed pressure gradient %—i.e., comparing the top and mid-row plots—leads to significantly smaller streaky structures, which appear thinner and characterized by a less regular motion along the streamwise direction. Moreover, the streak breakup is captured slightly upstream ($x/L = 0.55$, $t = t_2$). The effect of flow deceleration at a fixed low Reynolds number can be assessed by comparing the top and bottom rows ($Re_L = 70k$, $DR = 2.10$) of Fig. 6. Specifically, streaky structures characterized by the larger spanwise wavelength are observed, since $x/L = 0.33$. Aiming to provide a

quantitative characterization of the spanwise wavelength for the surveyed structures, spanwise autocorrelation functions of instantaneous flow fields have been computed on the wall-parallel plane at streamwise locations embedded within the transitional region. Results are shown in Fig. 7(a), focusing on the same flow conditions reported in Fig. 6, for conciseness. As well established in the literature,[39] the spacing between adjacent, opposite sign streaks is identified by the minimum of autocorrelation functions. Its accuracy directly relates to the measurement grid of the PIV system and corresponds to about $\Delta z/L = 0.0014$. The corresponding spanwise wavenumbers $\beta = 2\pi/\Delta z$ computed by autocorrelations are summarized in Fig. 7(b) for all the DR and Re_L investigated in this work. The PIV resolution on the wall parallel plane provides an overall uncertainty of the non-dimensional wave number $\Delta\beta = 15$. As can be noticed, the streak spanwise wave number increases with Re_L. This is mainly due to the corresponding reduction of the boundary layer thickness, which alters

15 March 2024 08:41:24
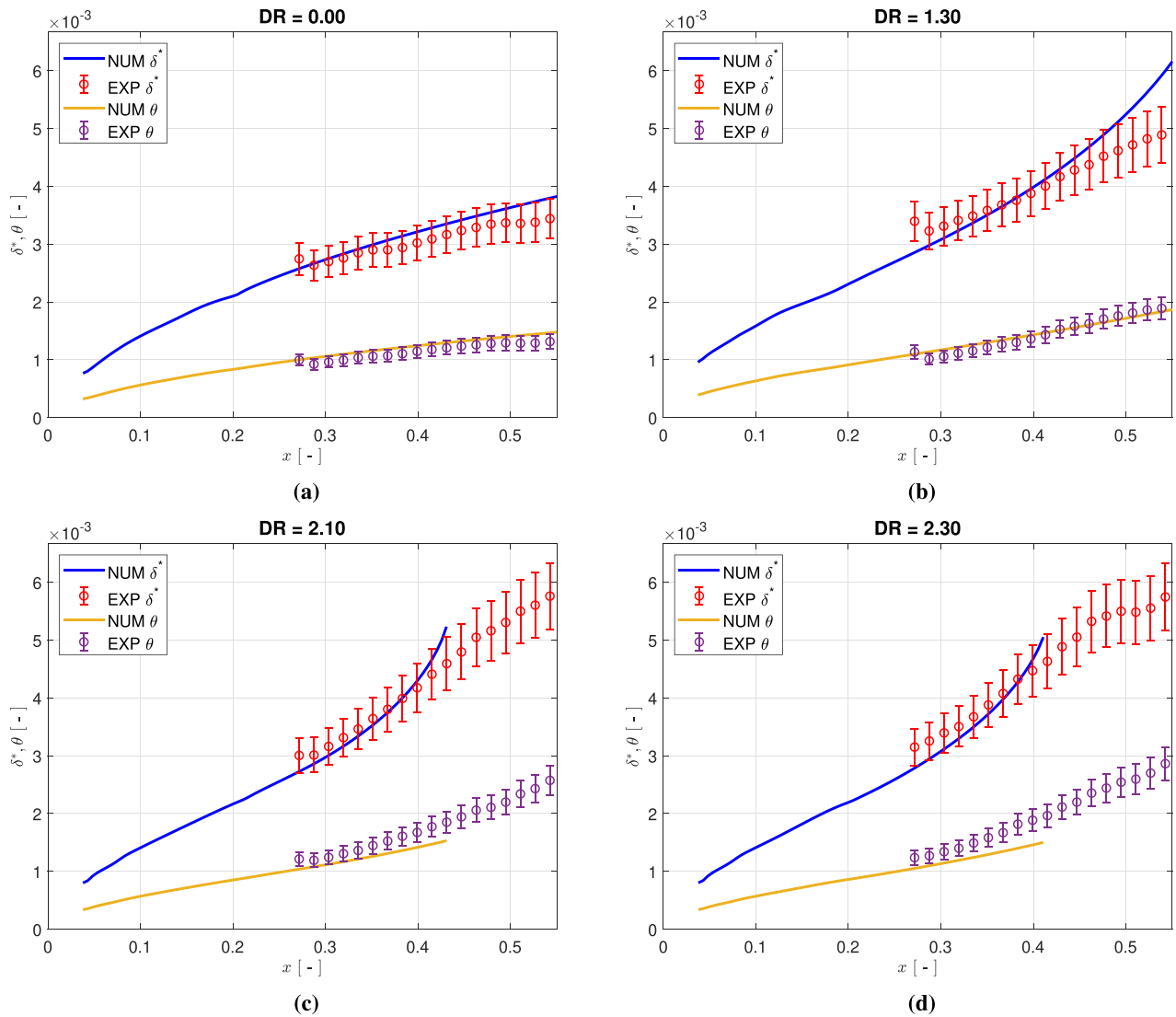
FIG. 5. Boundary layer integral parameters obtained by means of PIV measurements (markers) and by the boundary layer solver (solid lines). Curves for $Re_L = 70\,\text{k}$ and (a) $DR = 0.00$, (b) 1.30, (c) 2.10, and (d) 2.30. The reported non-dimensional plots follow the scaling indicated in Table II.

the boundary layer receptivity properties.[26] It is also shown that increasing DR reduces β, as illustrated in Fig. 7, and this effect tends to decline as Re_L rises, since the spanwise wavenumber settles close to 300 for both $Re_L = 150\,\text{k}$ and $Re_L = 220\,\text{k}$. Figures 7(c) and 7(d) report the peak of *rms* of the optimal perturbation streamwise velocity component u alongside the akin *rms* value from PIV measurements against the x coordinate for $Re_L = 70\,\text{k}$ and varying DRs. Error bars accounting for uncertainty on the PIV rms measurements are introduced, according to Kubacki *et al.*[33] The numerical inlet perturbation spanwise wavelength has been set from Fig. 7(b), thus ensuring comparability in terms of amplification. Similarly, the theoretical and experimental data are matched at the first experimental station to get detailed insight into the spatial growth of disturbances along x, regardless of the initial perturbation energy. Finally, the

streamwise evolution of numerical disturbances has been computed from the leading edge of the flat plate[13,15] up to the x positions where nonlinearities and turbulent breakdown start (see Sec. IV A). Overall, Figs. 7(c) and 7(d) shows good agreement between the amplification rates provided by linear stability theory and experiments, especially for $DR = 0.0$ and $DR = 1.3$. Nevertheless, the fictitious boundary layer separation detected by the numerical solver for nonzero DRs limits the x range where such comparison is achieved—especially for $DR = 2.10$ and $DR = 2.30$. The computed perturbations start to differ from the experimental data just upstream of the laminar boundary layer separation detected by the solver. Overall, the disturbance spatial growth agrees well with the evolution of the root mean square of the streamwise fluctuating velocity in the explored flow conditions.
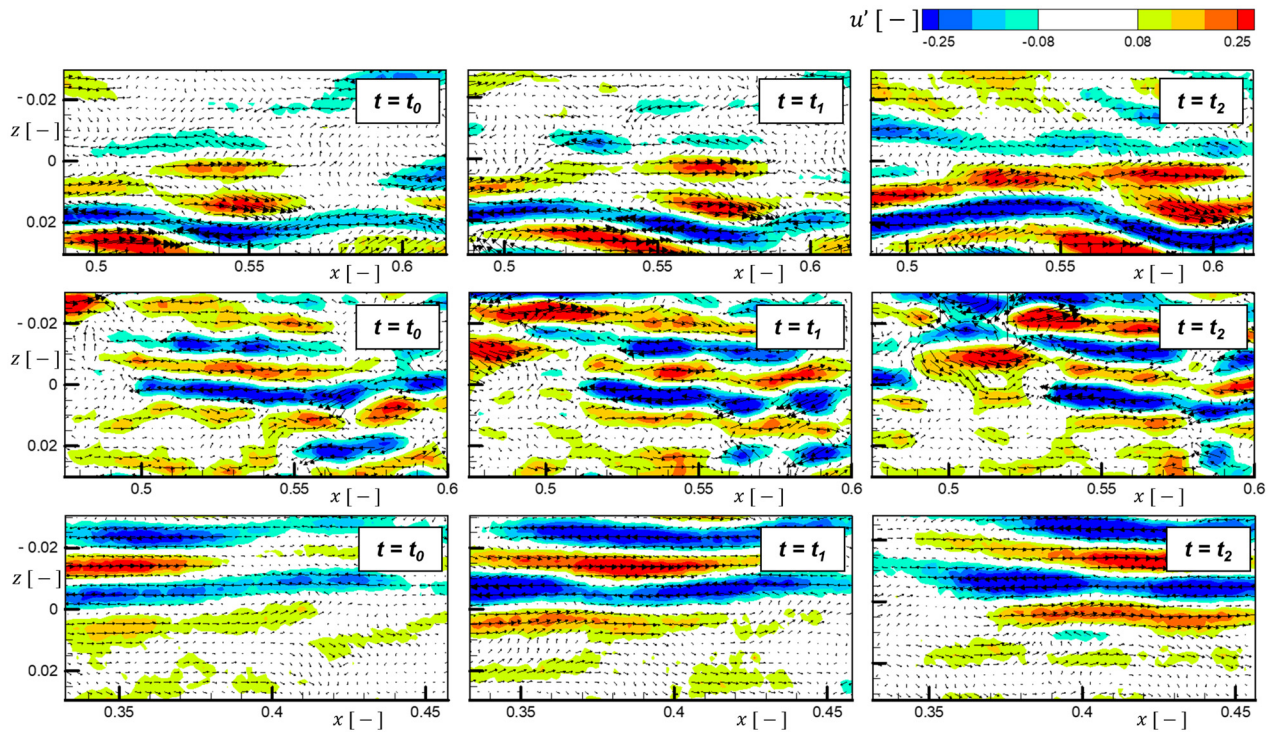
FIG. 6. Contour plots of the streamwise fluctuating component u' collected in the boundary layer wall parallel plane for $Re_L = 70\,k$, $DR = 0.00$ (top row), $Re_L = 220\,k$, $DR = 0.00$ (mid row), and $Re_L = 70\,k$, $DR = 2.10$ (bottom row). Three snapshots are shown for each condition at progressive time steps. Fluctuating velocity vectors are superimposed to the contour plots of the streamwise fluctuating component u'. The reported non-dimensional plots follow the scaling indicated in Table II.

C. Optimal disturbances and comparison with experiments

In the following, the outcome of a Design Of Experiment performed over a domain of variables composed of the spanwise wavenumber β, the inlet position x_i, and the final position x_f is described. The analysis is carried out for all the Re_L and DR flow conditions available from the experimental campaign. The dependence of the maximum transient growth G on the spanwise wave number is assessed in Fig. 8: the disturbance is introduced in the boundary layer near the flat plate leading edge, and its energy is maximized at the final position $x_f/L = 0.40$. The initial and final positions of the disturbance evolution are kept constant for all the different DRs, following the analysis of Sec. IV A. This allows us to avoid influences of the streamwise extension of the domain on the growth rate, as well as to perform computations within the laminar pre-transitional region of the flow. Figure 8 shows that all the curves detect a maximum G against β, as already observed for similarity-based boundary layer flows.[13,15,16] Furthermore, disturbance gain increases with APG, since higher pressure gradients destabilize the boundary layer and anticipate transition breakdown.[42] The effect of DR appears to be remarkably stronger for values ≥ 2.00, with little influence at high Re_L number flows. Indeed, for $Re_L = 150\,k$ and $220\,k$, the optimal β—i.e., the spanwise wavenumber maximizing G—tends to converge to a value between 200 and 300, interestingly in line with the experimental findings summarized in Figs. 7(a) and 7(b). In Fig. 8, it is also shown that a DR increase tends to slightly reduce the optimal β: this appears to be caused by the

boundary layer thickening at high APGs, which allows the receptivity of perturbations characterized by larger spanwise wavelengths.[43,44] Additionally, the destabilizing effect of Re_L on the perturbation spatial growth is shown in all plots, as the disturbance gain increases with Re_L. Perturbations characterized by large spanwise wavenumbers were also observed to grow faster in the streamwise direction for increasingly higher Re_L. Tendency curves were added to Fig. 8 for optimal perturbations obtained by linear stability theory (red dashed lines) and the experimentally surveyed streaks (yellow dashed lines). Additionally, the trend shown for the optimal βs and experimental data is similar for $DR = 0.00$ and $DR = 1.30$, despite showing different trend slopes with Re_L. Moreover, it is shown that optimal βs from linear stability theory and experimental values come closer at high DR for all Re_L—not observed otherwise, especially at $DR = 0.00$. Specifically, the optimal β values at $DR = 0.00$ are significantly lower than the corresponding experimental βs for all Re_L. The highlighted discrepancy may be due to the shear sheltering phenomenon acting on a real receptivity process to the free-stream turbulence.[43,44] Dellacasagrande et al.[45] showed in a previous work on the same database that the spanwise wavenumber of streaky structures approximately matches the boundary layer thickness (i.e., $\Delta z/\delta^* \approx \delta_{99}$), independently of the DR considered. On the contrary, the calculated optimal βs reported in Fig. 8 for $DR = 0.00$ correspond to streamwise disturbances exceeding the boundary layer thickness (e.g., $\Delta z \approx 3.6\delta_{99}$ for $Re_L = 70\,k$, $x/L = 0.40$). Thus, these perturbations were probably filtered out in the receptivity process taking place in the experiments.[43] On the other
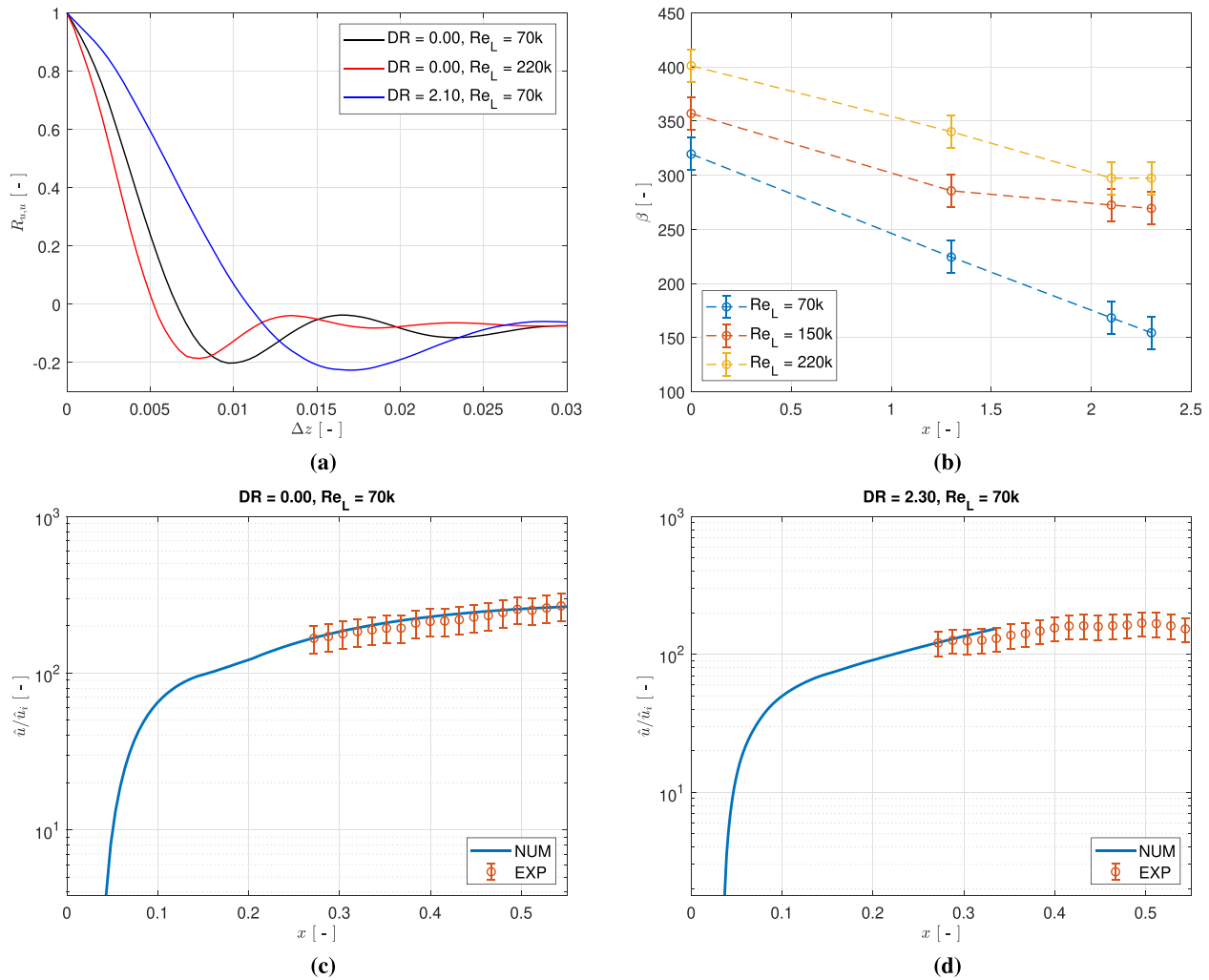
FIG. 7. (a) Spanwise autocorrelation functions of the streamwise velocity $\mathbf{R_{uu}} = \langle u'(z_0)u'(z_0 + z)\rangle/\langle u'^2\rangle$ highlighting the Re_L and the DR effect on the disturbance spanwise wavelength, (b) experimental spanwise wavenumber β obtained from the autocorrelations of PIV measurements, (c)–(d) evolution of numerical and experimental perturbation amplitude $\hat{u}$ along x-coordinate at fixed $Re_L = 70$ k and varying DR. The reported non-dimensional plots follow the scaling indicated in Table II.

hand, the receptivity process at non-zero DR appears to resemble the optimal one since good agreement exists between numerical and experimental results. Finally, the comparison against increasing DR is also affected by the boundary layer thicknesses themselves: at higher APG, thicker boundary layers allow for an overall better resolution than the lower or zero pressure gradient ones. Given all of the above, the optimal disturbances from linear stability theory are not detected consistently throughout all the flow conditions experimentally tested. Hence, the optimization of the inlet and final locations of the disturbance evolution performed in the following paragraph employs β values from experiments.

The effect of the final position x_f on the disturbance growth rate is reported in Fig. 9 for $Re_L = 70$ k and variable DR, with x_f ranging between $x/L = 0.17$ and 0.40. All the curves lie close to each other up to $x_f/L = 0.25$, approximately in the fixed fore accelerating part of the test section (see Sec. II). Instead, the adverse pressure gradient imposed

just downstream of the geometric throat ($x/L \geq 0.20$) by the diverging end-walls influences the boundary layer, causing G to increase. The effect is more prominent at higher DRs: all the curves differ significantly when $x/L > 0.25$. Additionally, it must be noticed that all the curves found are monotonic with x_f in the explored range, in contrast with previous findings from Andersson *et al.*[13] This discrepancy directly follows from the complex nature of the flows considered in the present work. Indeed, even the flow condition with $DR = 0.00$ differs from the Blasius similarity solution due to the accelerating boundary layer developing for $x/L < 0.20$, i.e., it is not a ZPG flow condition. In Figs. 10(a)–10(c), the dependency of the maximum spatial transient growth on the inlet position x_i—where the disturbance is introduced— is investigated against DR and Re_L. Gain is computed along the streamwise direction for different evolution lengths by varying the inlet location x_i up to $x/L = 0.33$, while the final optimization position is kept constant at $x/L = 0.40$. Interestingly, Figs. 10(a)–10(c) show that the

15 March 2024 08:41:24
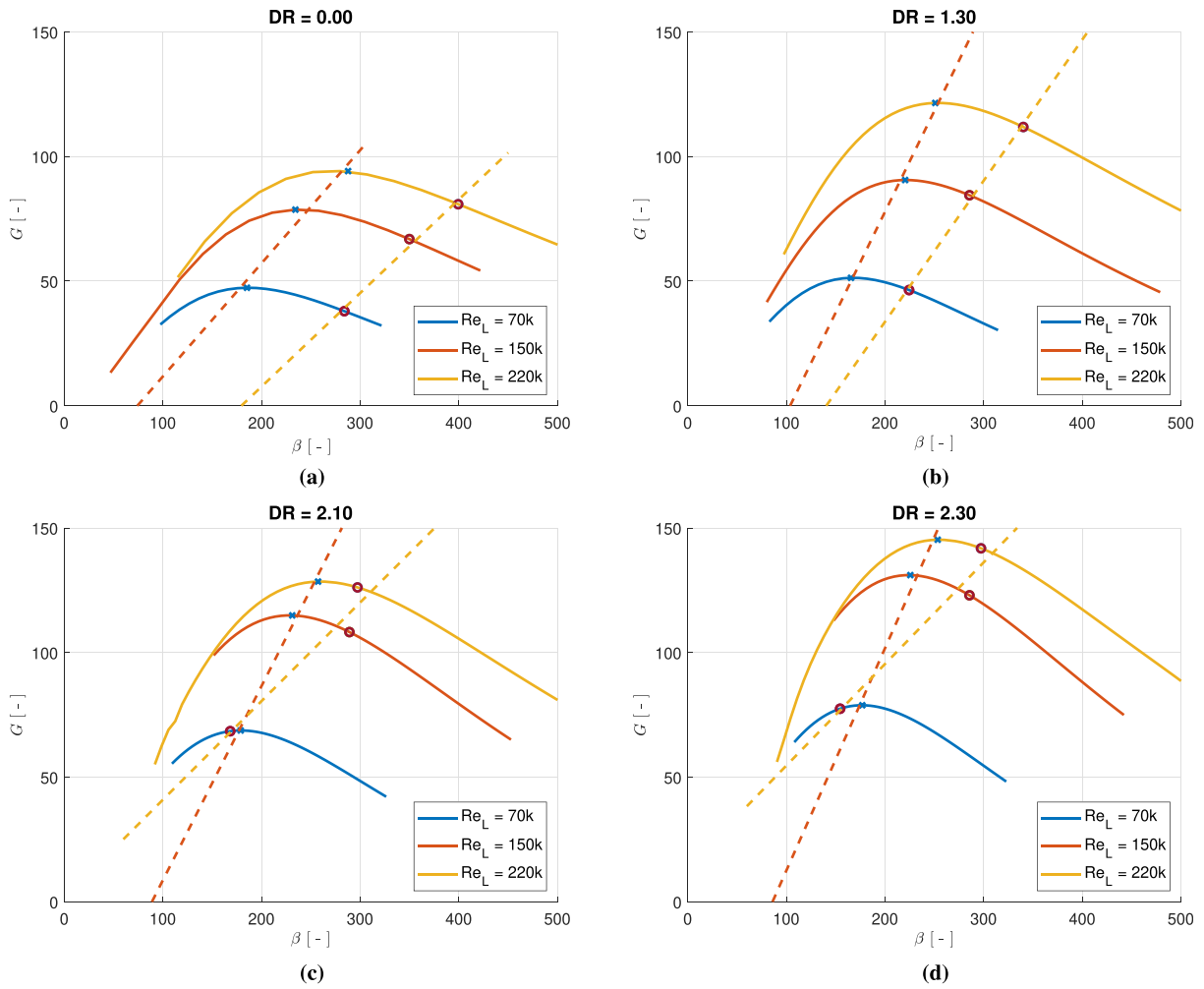
FIG. 8. Effect of β on gain for varying Re_L. Circular and cross markers locate experimental β and optimal disturbances, respectively. Tendencies for optimal perturbations (red dashed lines) and experimentally surveyed streaks (yellow dashed lines) are also shown.
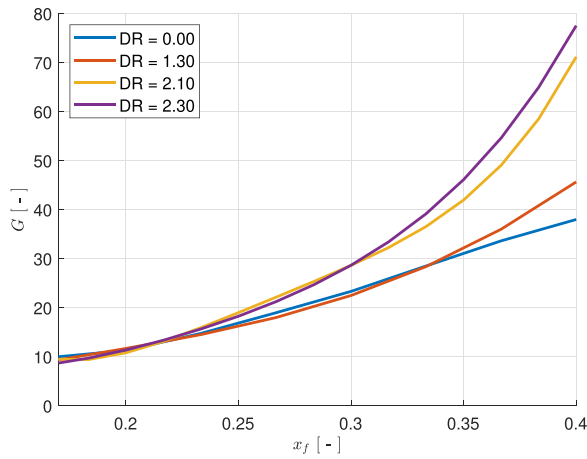
FIG. 9. Effect of the final position x_f on gain for varying DR. Results for $Re_L = 70$ k.

maximum spatial transient growth occurs when the disturbances penetrate the boundary layer slightly upstream of the geometric throat, with negligible influence from the DR.

Finally, the effect of x_i on the disturbance energy growth is depicted in Fig. 10(d) for $DR = 0.00$ and 2.30, and varying Re_L. As it can be seen, the optimal inlet position for the perturbations occurs approximately at the geometric throat at all the Re_L numbers accounted for. Therefore, the analysis of the inlet position x_i suggests that the maximum transient growth in the case of turbomachinery flows occurs for disturbances entering the boundary layer next to the geometric throat, almost independently of diffusion rates and Reynolds numbers.

V. CONCLUSIONS

The free-stream turbulence induced transition occurring under typical low-pressure turbine flow conditions has been investigated employing linear stability theory and compared to experimental data.
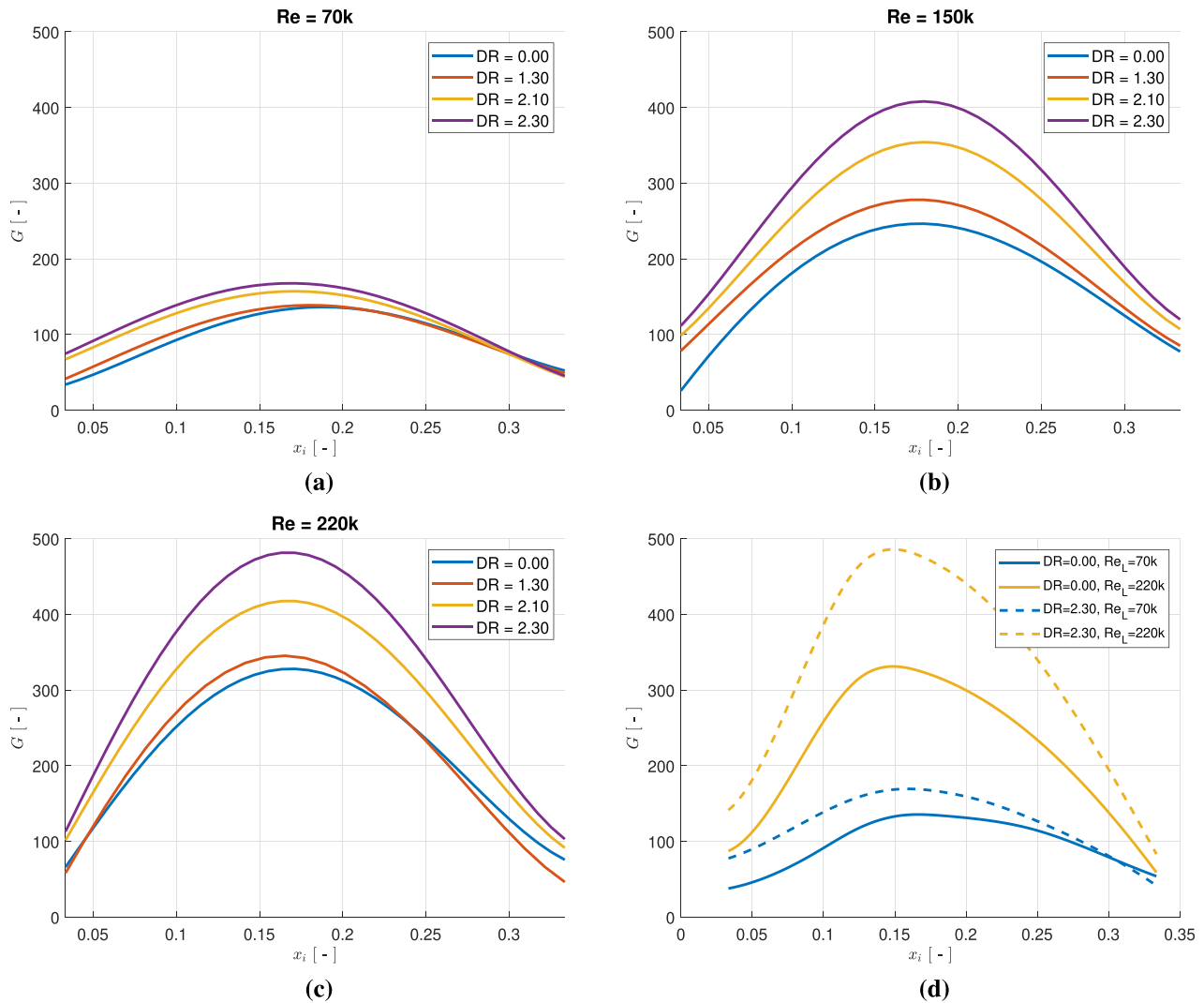
15 March 2024 08:41:24

FIG. 10. (a)–(c) Effect of the inlet position x_i on gain for varying DR at different Re_L, (d) effect of the disturbance inlet position x_i on gain for varying Re_L.

The analysis accounted for three different Reynolds numbers and four adverse pressure gradients.

First, a non-similarity-based boundary layer solver was used to compute base flows and validated against experimental data. The comparison showed good agreement within the laminar pre-transitional region in terms of free-stream velocity as well as boundary layer and rms profiles. Second, linear stability theory coupled with a direct-adjoint optimization procedure was applied to find optimal disturbances and their spatial transient growth for all the flow conditions considered. The sensitivity of the disturbance spatial transient growth to the spanwise wavenumber of perturbations, the receptivity position, and the location where disturbance energy is maximized were explored numerically.

Overall, the comparison against experimental particle image velocimetry measurements showed good agreement with the optimal perturbations computed by linear stability theory. More precisely, the disturbance spatial evolution obtained from numerical optimization was shown to approximate the one surveyed in experiments—especially for low DRs. Furthermore, the spanwise wavenumber of optimal disturbances was found to reduce for increasing DR, with weaker effect played at higher Re_L numbers, for both the numerical and experimental data. Interestingly, the spatial transient growth of optimal disturbances appeared to increase only monotonically with x_f and DR, due to the complex, non-similarity-based nature of the flow. Finally, the maximum energy growth of disturbances has been shown to occur for perturbations entering the boundary layer close to the geometrical throat position, almost independently of diffusion rates and Re_L numbers.

AUTHOR DECLARATIONS
Conflict of Interest

The authors have no conflicts to disclose.

Author Contributions

Alessandro Dotto, Matteo Luzzi, and Jacopo Verdoya contributed equally to this work.

Alessandro Dotto: Conceptualization (lead); Data curation (lead); Formal analysis (lead); Writing – original draft (lead); Writing – review & editing (lead). **Matteo Luzzi:** Conceptualization (lead); Data curation (lead); Formal analysis (lead); Writing – original draft (lead); Writing – review & editing (lead). **Jacopo Verdoya:** Conceptualization (lead); Data curation (lead); Formal analysis (lead); Writing – original draft (lead); Writing – review & editing (lead). **Daniele Simoni:** Supervision (lead); Writing – review & editing (lead). **Ardeshir Hanifi:** Supervision (lead); Writing – review & editing (lead). **Jan Oscar Pralits:** Supervision (lead); Writing – review & editing (lead).

DATA AVAILABILITY

The data that support the findings of this study are available from the corresponding author upon reasonable request.

NOMENCLATURE

C_p	pressure coefficient (-)
G	spatial transient growth (-)
i	imaginary unit
L	flat plate length (m)
L_{ref}	reference length (m)
p	pressure disturbance (-)
P	pressure (-)
q	disturbance vector (-)
Re_L	Reynolds number (-)
t	time (s)
Tu	turbulence intensity (%)
u, v, w	disturbance components (-)
U, V, W	base flow velocity components (-)
x, y, z	streamwise, wall-normal, and spanwise directions (-)
β	streaks spanwise wavenumber (-)
β_P	porosity parameter (-)
δ^*	boundary-layer displacement thickness (-)
θ	boundary-layer momentum thickness (-)
ν	kinematic viscosity (m^2/s)
ρ	density (kg/m^3)

Subscripts/Superscripts

e	external (free-stream)
f	final position
i	initial position
L	flat plate length
th	throat position
T	conjugate transpose
x, y, z	partial derivatives
$*$	adjoint
$\hat{}$	magnitude

Abbreviations

APG	adverse pressure gradient
BL	boundary layer
DNS	direct numerical simulation
DR	diffusion rate
FSC	Falkner–Skan–Cooke
FST	free-stream turbulence
LDV	laser doppler velocimetry
LPT	low-pressure turbine
PG	pressure gradient
PIV	particle image velocimetry
PSE	parabolized stability equations
ZPG	zero pressure gradient

APPENDIX: NUMERICAL PROCEDURE

The 2D steady boundary layer problem solved in the present work for the base flow $(U, V, 0)$ computation relies on the governing equations reported in the following:

$$\frac{\partial U}{\partial x} + \frac{\partial V}{\partial y} = 0,$$
$$U\frac{\partial U}{\partial x} + V\frac{\partial U}{\partial y} = -\frac{dP}{dx} + \frac{1}{Re}\frac{\partial^2 U}{\partial y^2}. \tag{A1}$$

Since the boundary layer profile near the leading of the flat plate was not available from experimental data because outside the PIV measurement domain, a Falkner–Skan similarity profile $U_e = x^m$ has been assumed as the inlet condition in Eq. (A1) to start computation. Specifically, the geometry of the flat plate leading edge has been used to estimate the local pressure gradient, i.e., the exponent m. Thus, this mathematical procedure overall solves laminar boundary layer equations without using the hypothesis of BL similarity since the free-stream evolution over the entire flat plate is complex and cannot be represented as $U_e = x^m$. However, a Falkner–Skan profile is used as the inlet condition in the leading region to ensure simplicity and reliability of the procedure, as it does not rely on DNS data, which is not within everyone's reach. A second-order backward finite difference scheme has been used to discretize Eq. (A1) along x for an overall amount of 200 discretization points over the entire flat plate length. Instead, a standard Chebyshev numerical scheme is adopted for the wall-normal direction following Hanifi et al.[31] Specifically, the authors considered the Chebyshev expansion

$$\phi(\eta) = \sum_{n=0}^{N} \hat{\phi}_n T_n(\eta) = \sum_{n=0}^{N} \hat{\phi}_n \cos\left(n \cos^{-1}(\eta)\right), \tag{A2}$$

where $T_k(\eta)$ is the Chebyshev polynomial of degree k defined over $\eta \in [-1, 1]$ and discretized it over collocation points $\eta_j = \cos(\pi j/N)$ for $j = 0, 1, \ldots, N$. Successively, the conformal mapping introduced by Hanifi et al.[31] was used to transform the interval $[-1, 1]$ into the computational domain $y \in [0, y_{\max}]$. Overall, 150 Chebyshev nodes were used along the wall-normal direction, as this value ensured to reach convergence on the Blasius boundary layer profile and the related optimal disturbances reported in Andersson et al.[13] The discretized equations are then integrated, imposing no-slip on the plate and local free-stream velocity $U_e(x)$ as boundary conditions, at $y = 0$ and $y = y_{\max}$, respectively. At each streamwise position, convergence is checked by employing the continuity equation: settings provide a 10^{-8} accuracy for the base flow numerical profiles.

The same discretization schemes have been used to solve direct (2) and adjoint (7) problems.

REFERENCES

[1]P. Durbin, "Perspectives on the phenomenology and modeling of boundary layer transition," Flow. Turbul. Combust. **99**, 1–23 (2017).

[2]H. P. Hodson and R. J. Howell, "The role of transition in high-lift low-pressure turbines for aeroengines," Prog. Aerosp. Sci. **41**, 419–454 (2005).

[3]P. S. Klebanoff, K. Tidstrom, and L. Sargent, "The three-dimensional nature of boundary-layer instability," J. Fluid Mech. **12**, 1–34 (1962).

[4]P. S. Klebanoff, "Effect of free-stream turbulence on the laminar boundary layer," Bull. Am. Phys. Soc. **10**, 1323 (1971).

[5]J. Hoepffner, L. Brandt, and D. S. Henningson, "Transient growth on boundary layer streaks," J. Fluid Mech. **537**, 91–100 (2005).

[6]H. W. Emmons, "The laminar-turbulent transition in a boundary layer-part I," J. Aeronaut. Sci. **18**, 490–498 (1951).

[7]P. Andersson, L. Brandt, A. Bottaro, and D. S. Henningson, "On the breakdown of boundary layers streaks," J. Fluid Mech. **428**, 29–60 (2001).

[8]J. Hunt and P. Durbin, "Perturbed vortical layers and shear sheltering," Fluid Dyn. Res. **24**, 375 (1999).

[9]T. A. Zaki and S. Saha, "On shear sheltering and the structure of vortical modes in single-and two-fluid boundary layers," J. Fluid Mech. **626**, 111–147 (2009).

[10]L. Brandt, F. Schlatter, and D. S. Henningson, "Transition in boundary layers subject to free-stream turbulence," J. Fluid Mech. **517**, 167–198 (2004).

[11]M. J. P. Hack and T. Zaki, "Data-enabled prediction of streak breakdown in pressure-gradient boundary layers," J. Fluid Mech. **801**, 43–64 (2016).

[12]P. Schlatter, L. Brandt, H. De Lange, and D. S. Henningson, "On streak breakdown in bypass transition," Phys. Fluids **20**, 101505 (2008).

[13]P. Andersson, M. Berggren, and D. Henningson, "Optimal disturbances and bypass transition in boundary layers," Phys. Fluids **11**, 134–150 (1999).

[14]F. Bertolotti, "Response of the blasius boundary layer to free-stream vorticity," Phys. Fluids **9**, 2286–2299 (1997).

[15]P. Luchini, "Reynolds-number independent instability of the boundary layer over a flat surface," J. Fluid Mech. **404**, 289–309 (2000).

[16]O. Levin and D. Henningson, "Exponential vs algebraic growth and transition prediction in boundary layer flow," Flow, Turbul. Combust. **70**, 183–210 (2003).

[17]E. R. V. Driest and C. Blumer, "Boundary layer transition: Freestream turbulence and pressure gradient effects," AIAA J. **1**, 1303–1306 (1963).

[18]P. V. Corbett and A. Bottaro, "Optimal perturbations for boundary layers subject to stream-wise pressure gradient," Phys. Fluids **12**, 120–130 (2000).

[19]J. O. Pralits and A. Hanifi, "Optimization of steady suction for disturbance control on infinite swept wings," Phys. Fluids **15**, 2756–2772 (2003).

[20]N. Abdessemed, S. Sherwin, and V. Theofilis, "Linear instability analysis of low-pressure turbine flows," J. Fluid Mech. **628**, 57–83 (2009).

[21]M. Zauner, N. D. Sandham, A. P. S. Wheeler, and R. D. Sandberg, "Linear stability prediction of vortex structures on high pressure turbine blades," Int. J. Torbomach. Propul. Power **2**, 8 (2017).

[22]X. Mao, T. Zaki, S. J. Sherwin, and H. Blackburn, "Transition induced by linear and nonlinear perturbation growth in flow past a compressor blade," J. Fluid Mech. **820**, 604–632 (2017).

[23]D. Simoni, D. Lengani, M. Dellacasagrande, S. Kubacki, and E. Dick, "An accurate data base on laminar-to-turbulent transition in variable pressure gradient flows," Int. J. Heat Fluid Flow **77**, 84–97 (2019).

[24]M. Dellacasagrande, J. Verdoya, D. Barsi, D. Lengani, and D. Simoni, "Dynamic mode decomposition analysis of separated boundary layers under variable reynolds number and free-stream turbulence," in ASME Turbo Expo 2020: Turbomachinery Technical Conference and Exposition, 21–25 September 2020 (ASME, 2020).

[25]M. Berrino, D. Simoni, M. Ubaldi, P. Zunino, and F. Bertini, "Off-design performance of a highly loaded LP turbine cascade under steady and unsteady incoming flow conditions," in ASME Turbo Expo 2014: Turbine Technical Conference and Exposition, Düsseldorf, Germany, 16–20 June 2014 (ASME, 2014).

[26]J. Verdoya, M. Dellacasagrande, D. Barsi, D. Lengani, and D. Simoni, "Identification of free-stream and boundary layer correlating events in free-stream turbulence induced transition," Phys. Fluids **34**, 014109 (2022).

[27]M. Dellacasagrande, D. Barsi, D. Lengani, D. Simoni, and J. Verdoya, "Response of a flat plate laminar separation bubble to Reynolds number, free-stream turbulence and adverse pressure gradient variation," Exp. Fluids **61**, 128 (2020).

[28]A. Sciacchitano, D. R. Neal, B. L. Smith, S. O. Warner, P. P. Vlachos, B. Wieneke, and F. Scarano, "Collaborative framework for piv uncertainty quantification: Comparative assessment of methods," Meas. Sci. Technol. **26**, 074004 (2015).

[29]B. Wieneke, "PIV uncertainty quantification from correlation statistics," Meas. Sci. Technol. **26**, 074002 (2015).

[30]J. Verdoya, M. Dellacasagrande, D. Lengani, D. Simoni, and M. Ubaldi, "Inspection of structures interaction in laminar separation bubbles with extended proper orthogonal decomposition applied to multi-plane particle image velocimetry data," Phys. Fluids **33**, 043607 (2021).

[31]A. Hanifi, P. Schmid, and D. Henningson, "Transient growth in compressible boundary layer flow," Phys. Fluids **8**, 826–837 (1996).

[32]L. Brandt and D. S. Henningson, "Transition of streamwise streaks in zero-pressure gradient boundary layers," J. Fluid Mech. **472**, 229–261 (2002).

[33]S. Kubacki, D. Simoni, D. Lengani, M. Dellacasagrande, and E. Dick, "Extension of an algebraic intermittency model for better prediction of transition in separated layers under strong free-stream turbulence," Int. J. Heat Fluid Flow **92**, 108860 (2021).

[34]P. Hammerton and E. Kerschen, "Boundary-layer receptivity for a parabolic leading edge," J. Fluid Mech. **310**, 243–267 (1996).

[35]N. Lin, H. Reed, and W. Saric, "Effect of leading-edge geometry on boundary-layer receptivity to freestream sound," in Instability, Transition and Turbulence (Springer, New York, 1992), pp. 421–440.

[36]J. M. Kendall, "Experimental study of disturbances produced in a pre-transitional laminar boundary layer by weak freestream turbulence," in 18th Fluid Dynamics and Plasmadynamics and Lasers Conference (AIAA, 1985).

[37]J. M. Kendall, "Boundary layer receptivity to freestream turbulence," in 21st Fluid Dynamics, Plasma Dynamics and Lasers Conference (AIAA, 1990).

[38]K. J. A. Westin, A. V. Boiko, B. G. B. Klingmann, V. V. Kozlov, and P. H. Alfredsson, "Experiments in a boundary layer subjected to free stream turbulence. part 1. boundary layer structure and receptivity," J. Fluid Mech. **281**, 193–218 (1994).

[39]M. Matsubara and P. H. Alfredsson, "Disturbance growth in boundary layers subjected to free-stream turbulence," J. Fluid Mech. **430**, 149–168 (2001).

[40]A. Dotto, D. Barsi, D. Lengani, and D. Simoni, "A data-driven optimal disturbance procedure for free-stream turbulence induced transition," Phys. Fluids **34**, 124108 (2022).

[41]G. B. Schubauer and H. K. Skramstad, "Laminar-boundary-layer oscillations and transition on a flat plate," J. Res. Natl. Bur. Stand. **38**, 251 (1947).

[42]K. P. Nolan and T. A. Zaki, "Conditional sampling of transitional boundary layers in pressure gradients," J. Fluid Mech. **728**, 306–339 (2013).

[43]T. A. Zaki and P. A. Durbin, "Mode interaction and the bypass route to transition," J. Fluid Mech. **531**, 85–111 (2005).

[44]D. Hernon, E. Walsh, and D. Mc. Eligot, "Experimental investigation into the routes to bypass transition and the shear-sheltering phenomenon," J. Fluid Mech. **591**, 461–479 (2007).

[45]M. Dellacasagrande, D. Lengani, D. Simoni, J. O. Pralits, K. Durovich, A. Hanifi, and D. S. Henningson, "Statistical characterization of free-stream turbulence induced transition under variable reynolds number, free-stream turbulence, and pressure gradient," Phys. Fluids **33**, 094115 (2021).

15 March 2024 08:41:24